3 Flight of the MSSTA III

3.1 Construction

The MSSTA payload and team arrived at White Sands Missile Range, New Mexico on March 17, 2002. The instrument flew on April 30, more than six weeks later. That interval was filled with more challenges and catastrophes than are typically encountered by half a dozen different payloads in succession, and the fact that the MSSTA was able to fly at all, let alone succeed as well as it did, is a testament to the hard work of my colleagues Dennis Martínez-Galarce, TJ Bay, Ramesh Kumar and AmirAli Talasaz, and the dedication and skill of the NASROC support personnel at White Sands. I will here describe the aspects of payload integration most relevant to understanding the data, and then present the results of the flight itself.

3.1.1 OPTICS

The multilayer-coated mirrors of the Ritchey-Chrétien telescopes were integrated into their optical tube assemblies and bench tested in the MSSTA cleanroom at Stanford after calibration measurements were completed at the ALS (The Herschelian telescopes consist of a single mirror and a camera, and thus cannot be tested as a unit until they have been integrated into the payload itself; they were not aligned until we reached White Sands Missile Range. Because none of these telescopes produced an image, the procedure used to align and test them will not be discussed in detail).

Each Ritchey-Chrétien OTA was tested in two ways: first, immediately after assembly, it was mounted in a Fizeau interferometer in order to sample its wavefront performance. Interferograms were collected using a CCD camera; because the interferometer set-up included two passes through the telescope, the interferograms were twice as sensitive as the Ronchigrams produced by

star-testing telescopes (*i.e.* one fringe corresponds to ¼ wave error). The interferometer system and a representative interferogram are shown in Figure 51. The interferograms were analyzed by eye to give an estimate of the overall level of aberration in the system, and to look for indications of how the performance might be improved. The optics were then tilted in order to minimize coma, rotated in order to optimize matching of the primary and secondary mirrors, and roughly set for focus.

In general, the telescopes performed at roughly the ¼ wave level; that is, they displayed enough aberrations that it is unreasonable to expect them to come close to the theoretical in-band diffraction limit of 0.1 arc-seconds. The interferometer revealed some pinching of the secondary mirrors in their cells on the small Ritchey-Chrétiens (171 Å and 180 Å); we were able to re-mount the 180 Å telescope in a new cell, but the 171 Å secondary was wedged in place and the problem could not be solved. We also discovered some curious distortions around the edge of the primary mirror of the 256 Å telescope, due to either strain from the Silastic putty holding the mirror in place or degradation of the multilayer stack. We constructed an aperture mask for the 256 Å telescope to prevent scattered light from the mirrors edge from contaminating the rest of the image.

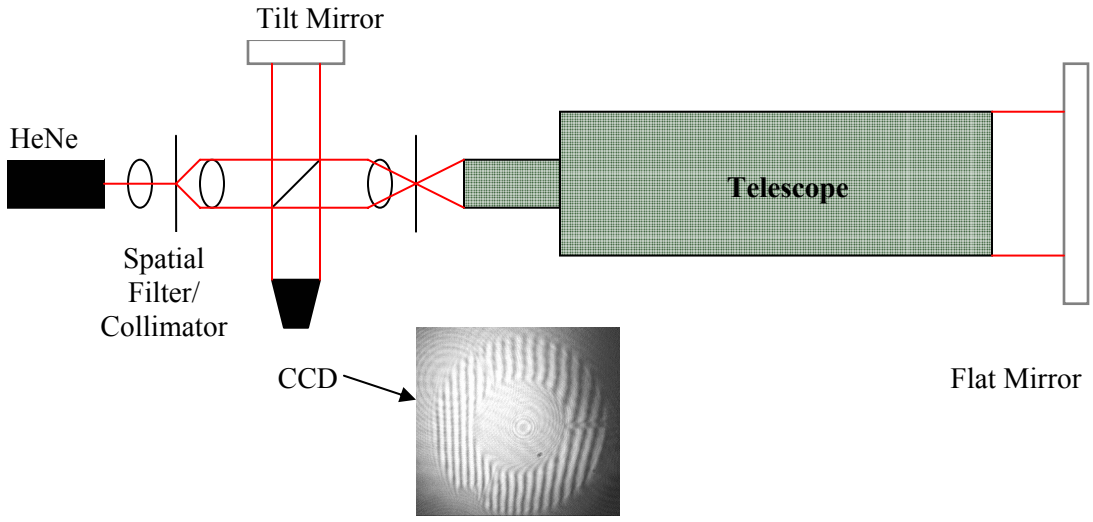

Figure 51. Schematic of the Fizeau interferometer used to assess the wavefront error of the MSSTA Ritchey-Chrétien telescopes. Also shown here is the interferogram of the 211 Å telescope, indicating reasonably smooth optics with some mild coma. This telescope was one of the best performers on the interferometer.

The telescopes were then placed in front of a 12" Cassegrain collimator, which projected a 1951 Air Force resolution test target into the aperture of the Ritchey-Chrétien. The instrument's camera was mounted, and images of the test target were taken on fine-grained SO-253 emulsion (as noted in Section 2.5, the SO-253 is not sensitive enough to EUV radiation for use in flight, but its excellent resolution capabilities ensure that it is not the limiting factor if it is used during alignment). The test target images were used to achieve final focus of the telescope. The OTAs are designed to allow focusing by using adjustment screws to push on the back of the primary mirror in order to affect small changes in its position; unfortunately, we discovered during interferometric testing that these screws stressed the mirrors and distorted the images, so we were forced to focus by shimming the cameras on the back of the telescope. We would set the camera in place, take a picture of the test target, change the shim controlling the focal plane position, and re-shoot the test target. The shim setting giving the best resolution performance was used during flight.

One detail that was not accounted for in past MSSTA flights: while the EUV telescopes use thin-film filters, the FUV telescopes (1550 Å and 1216 Å) use interference filters on 4mm thick MgF_2 substrates. Passing the converging beam of the telescope through a refractive medium results in a backward shift of the focal plane; using Snell's law, we find that a filter of thickness t and index of refraction n_R at the telescope's operating wavelength pushes the focal plane back by

$$s = \left(1 - 1/n_R\right)t$$

The telescopes are focused at visible light; if the effect of the filter is not compensated for, the focal plane will be found >1mm in front of its optimal position for flight, resulting in an increase in the spot size of > 100 μm (about 6 arc-seconds at the focal plane of the Ritchey-Chrétien telescopes). While this may account for some of the blurring seen in earlier MSSTA FUV images, we compensated for it by using CaF_2 blanks (whose visible-light n_R is close to the FUV n_R of MgF_2) during visible-light focus testing. The slight increase in longitudinal spherical aberration due to the presence of the filter is not a significant concern.

Central Wavelength [Å]	Resolution [arc-seconds]
58	15
98	8
131	12
150	8
171	20
180	2.5
195	2.5
211	1.8
256	6
1216	1.5
1550	1.5

Table 13. Pre-flight measurements of telescope resolution. The collimator used to project the test targets was limited to ~1.5 arc-seconds, so the sharper MSSTA telescopes (particularly the FUV instruments, as well as the 211 Å and 195 Å) may have outperformed these estimates.

Some of the alignment was re-done (or done for the first time) at WSMR, and final test-target images were taken with each telescope after shake-testing of the payload. Examining the tests under a microscope gave a pre-flight estimate of the resolving power of each telescope. The results are shown in Table 13. The resolution estimates given there are less optimistic than those given for the MSSTA II telescopes in (Martínez-Galarce, Walker et al. 2000); however, in both cases the resolution of the images is ultimately limited, not by the optical performance of the telescopes, but by the film grain.

3.1.2 ELECTRONICS

The flight electronics were substantially similar to the configuration flown on the MSSTA II (Martínez-Galarce 2000). The design consists of four custom-made circuit boards in isolated housings at the back of the payload truss: the analog board handled the power distribution to the payload, the IMP board contained the main microprocessor and was responsible for control and telemetry, and two camera boards were constructed to relay signals to and from the custom-built control boxes on the Pentax 645 cameras. Several minor updates and IC replacements were made on the electronics boards by AmirAli Talasaz and Ramesh Kumar; the changes are detailed in the Appendix.

The flight software, on the other hand, was almost completely rewritten after a series of bugs and incompatibilities were identified in the latest available version of the software. This was a major undertaking, and was only completed three days prior to launch. The principle revisions consisted of the addition of several layers of redundancy to the camera control system. In addition to the running a pre-loaded exposure sequence, stored in EEPROM on the camera boards, we gave the flight computer the ability to reset individual cameras, and to respond to manual camera firing commands from the ground. All of these capabilities would be required during flight.

3.1.3 PAYLOAD INTEGRATION

Most of the delicacy required in integration of the payload is necessary in order to protect the EUV thin-film filters. They are the reason that the payload must be evacuated during launch, so that vibrations induced by the rocket motors or the explosive decompression of the payload when the shutter door opens do not cause the filters to rupture. In order to minimize the chance of damage to the delicate EUV filters, they were not tested until the day before the payload was buttoned up for flight.

The Ritchey-Chrétien optical tubes were integrated into the payload truss and coaligned with a 16” collimator, using the sun sensor for the SPARCS attitude control system as a reference. Mechanical integration and alignment of the Herschelian telescopes was re-checked with the same collimator.

The full list of instruments included on the MSSTA III is shown in Table 1. A view of the payload from the sun’s perspective just prior to its integration with the telemetry system is shown in Figure 52.

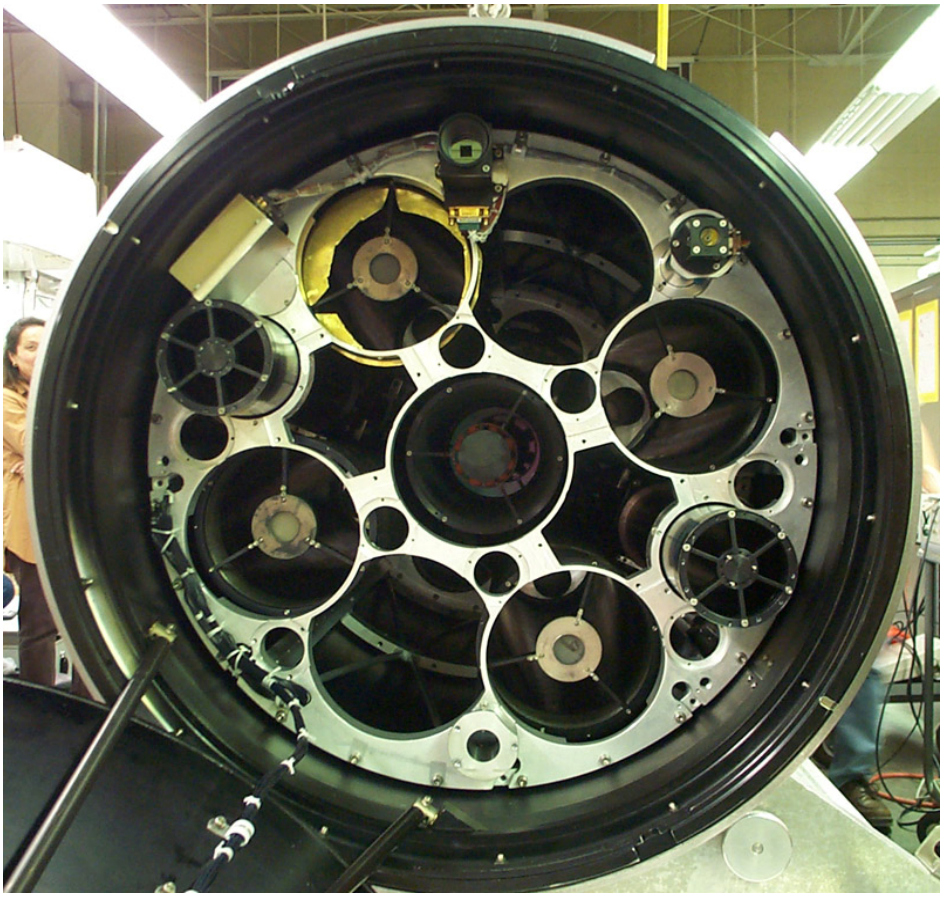

Figure 52. Sun's-eye view of the MSSTA III.

3.1.4 FLIGHT PERFORMANCE

High winds on the day of flight threatened to cause the MSSTA to miss its launch window. We were forced push the launch time back by half an hour (resulting in a lack of simultaneity between the flight and the supporting EIT and TRACE observations) and were on the point of scrubbing the launch when a break in the winds was verified. The payload launched at 12:25 pm MDT (18:25:00 UTC). The two-stage, Terrier-boosted Black Brant launch vehicle gave the payload an apogee of 270.5 km, resulting in more than five minutes of observing time.

Shortly after the start of the exposure sequence, MSSTA telemetry reported that current spikes from the 1550 Å camera had caused the flight electronics to shut that camera off. We were forced to reset the camera board. At that point, we lost reliable telemetry from the instrument altogether

(though telemetry from the power supply and flight guidance systems was not interrupted). We made the decision to activate manual control of the camera firing sequence. Therefore, all the exposures were made in response to me pressing a button in the control room at WSMR. The exposure times of the images were thus not as accurately-defined as they would be had the software-encoded exposure sequence run properly. We reconstructed the exposure times to 0.1-second precision by examining the post-flight log of current flow out of the main battery to the instrument; current spikes indicate the end of each exposure, as the camera advances the film to the next frame.

Nevertheless, the vehicle and the instrument performed well. Upon recovery, the payload showed signs of a rough landing. It had bounced and dragged on its parachute, and the waist vacuum was broken, sucking sand into the payload interior. However, despite the ominous sounds of sand and loose rivets rattling around inside the payload skin, everything was essentially intact.

The log of flight events and a summary of the payload telemetry is included in the appendix. They indicate that the SPARCS ACS performed within its specifications throughout the flight, with the largest excursions occurring during the 100 second exposure. The summary of flight data is based on information supplied by (NASROC 2002).

3.2 The Dataset

After recovery of the payload, the payload skin was opened and the camera backs were unloaded in the darkened alignment room at WSMR. Once we had verified that none of the cameras had broken on landing, the film was transferred to the darkroom of the journalism department of New Mexico State University, where it was developed in the JOBO film processor. Meanwhile, the payload itself was removed from its skins and examined for damage. The failure of the filters on the 58 Å, 98 Å and 131 Å telescopes was immediately noted. However, seven of the other eight telescopes performed well, and recorded multiple images over the course of the flight. These results are presented in the following section.

3.2.1 FILM DEVELOPMENT AND CLEANING

All negatives were developed with the same process based on our film calibration work at SSRL: 10 minutes in Kodak D-19, followed by a stop bath and rinse, then 5 minutes in Kodak Rapid Fixer, and finally a 20 minute rinse in running water. All chemistry was held at 20° C during processing. The negatives were dried overnight. Photo-flo was not used due to concerns about its effect on repeatability; this turned out to be a mistake, as some of the negatives show notable water-spotting.

Worse, the negatives suffer from extensive cracking and clumping in the film grain. As mentioned in Section 2.5, the photographic film used on the MSSTA flight was roughly 10 years old, and showed some signs of degradation in both sensitivity and grain structure. Furthermore, the XUV-100 has always shown a tendency to dry and crack under vacuum, producing heavy dark lines when the negatives are scanned. Software was developed to remove the worst of the damage (see the IDL code for PB_DESCRATCH and PB_DUSTBUSTER in the Appendix). It works by taking the derivative of the image in the direction perpendiculat to the scratches (during descratching) or the Laplacian of the image (during dust removal), thresholding and blurring the result to create a bad pixel mask, and replacing pixels in the mask with pixel values based on the

pixels around the boundary of each excised region. The results are shown in Figure 53; the loss of data cannot be prevented, but the scratches no longer contaminate attempts to measure average pixel values in a given region of the image.

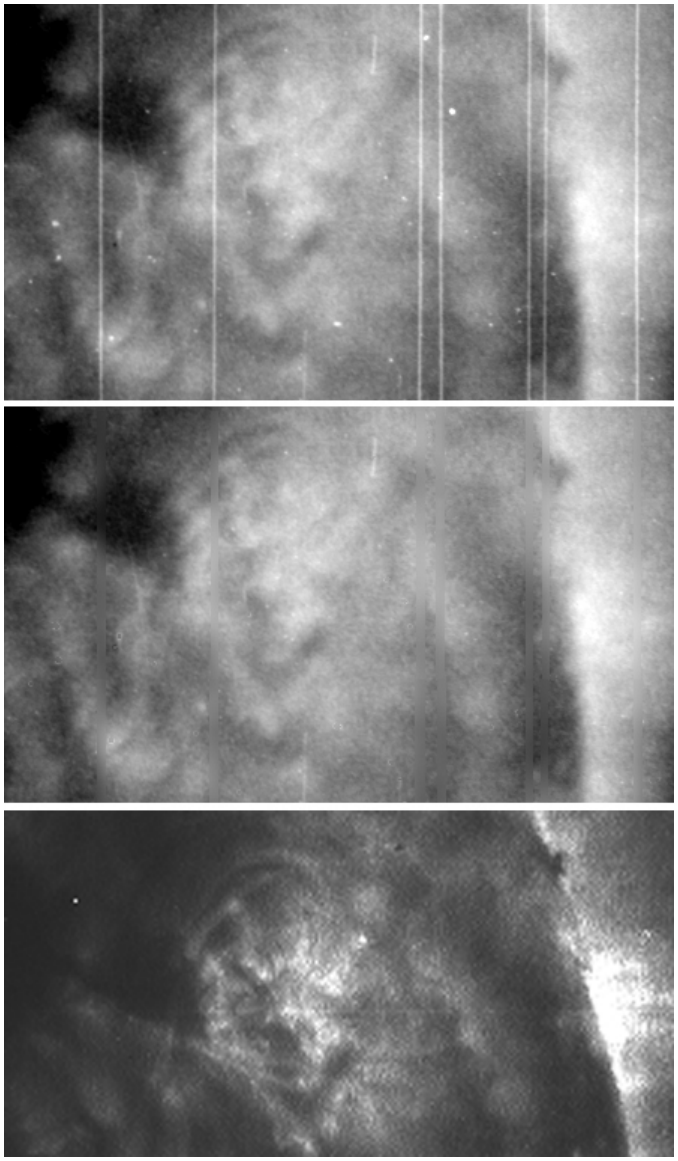

Figure 53. MSSTA images, like the 195 Å 40-second exposure shown here, suffer from film cracking as well as dust and scratches *(top)*. IDL descratching and dustbusting alleviated these problems *(middle)*. Nevertheless, image resolution was comparable to, or slightly worse than, that of EIT's 195 Å telescope *(bottom)*.

The negatives were digitized using a Umax film scanner with 1200 dpi nominal resolution; testing the scanner with a 1951 resolution target suggest its true resolution is close to nominal

perpendicular to the motion of the scanning assembly, and better than ~1000 dpi in the direction of motion. Considerable time was spent digitizing the images with a much more expensive Imacon Flextight Photo Scanner with a nominal resolution of 3200 dpi; unfortunately, while the Imacon scanner performed beautifully over small regions of the image, it was unable to scan a full 4.5 cm negative without introducing unacceptable distortions in the scanning direction. The problem defied several trips to the manufacturer for adjustment, and finally the Imacon scanner was abandoned.

Linearity of the Umax scanners measurements was tested, but is ultimately irrelevant given the film calibration procedure we used, which bypasses pixel value-to-density conversion. As long as the scanner gives repeatable measurements, which it seems to do, linearity is not necessary.

3.2.2 IMAGE COALIGNMENT

Because the MSSTA telescopes are independently mounted in the payload (unlike the TRACE telescope quadrants), and because the digitized images are scanned manually, image coalignment is a significant challenge. The digitized images were coaligned manually by placing green tag markers at ~20 points around the limb of the solar disk in Photoshop. The tagged image was then read in, and an oblate solar disk was fit to the marked limb points. The center coordinates of the resulting disk were used to establish a fiducial point in each scanned negative. The radius of the best-fit limb was not used to correct the image scale of the telescopes, in order to avoid concerns about the varying height of the limb in different bandpasses. The images were then superimposed on a reference EIT image and rotated around their centers in 0.1° increments until the best correlation was found. The resulting image center and rotation angles were stored in the FITS header of each exposure.

3.2.3 RESOLUTION ANALYSIS

On microscopic examination of the flight images, it was immediately apparent that the grain of the XUV-100 film limited the resolution of the EUV images. None of these images came close to

the resolution predicted by their performance on the interferometer or under pre-flight alignment testing with SO-253 film. The grain of the film is quite evident. Quantifying the image degradation caused by the film is simple: a sharp edge between two large regions of uniform density was found by examining the edge of the frame of one of the scanned negatives. The image was summed in the direction parallel to the edge, and the slope of the pixel value curve across the transition indicates the steepness of the film's contrast transfer function. This test indicates that the XUV-100's resolution in flight was roughly 6.5 arc-seconds at the focal plane of the large Ritchey-Chrétien telescopes (and about 11 arc-seconds for the small Ritchey-Chrétien 171 Å and 180 Å instruments). This finding is supported by comparison of the MSSTA images with EIT images in similar bandpasses (see Figure 53). EIT's nominal (pixel-limited) resolution is about 5 arc-seconds.

The FUV images, taken on ultra-fine-grained S-649, fared far better, and essentially reproduced the results of the pre-flight resolution tests. The 1550 Å image displays resolution only slightly worse than TRACE's 1550 Å bandpass, which is pixel-limited at about 1 arc-second.

3.2.4 THE IMAGES

The MSSTA III dataset consists of 84 images in 7 different EUV and FUV bandpasses. An image from each of these bandpasses is presented below, along with a discussion of the important characteristics of each telescope's performance. In all cases, solar North is up; for the EUV images, the results presented here are all 40-second exposures taken near apogee. They have been thresholded and downsized, decreasing their dynamic range and (in some cases) resolution.

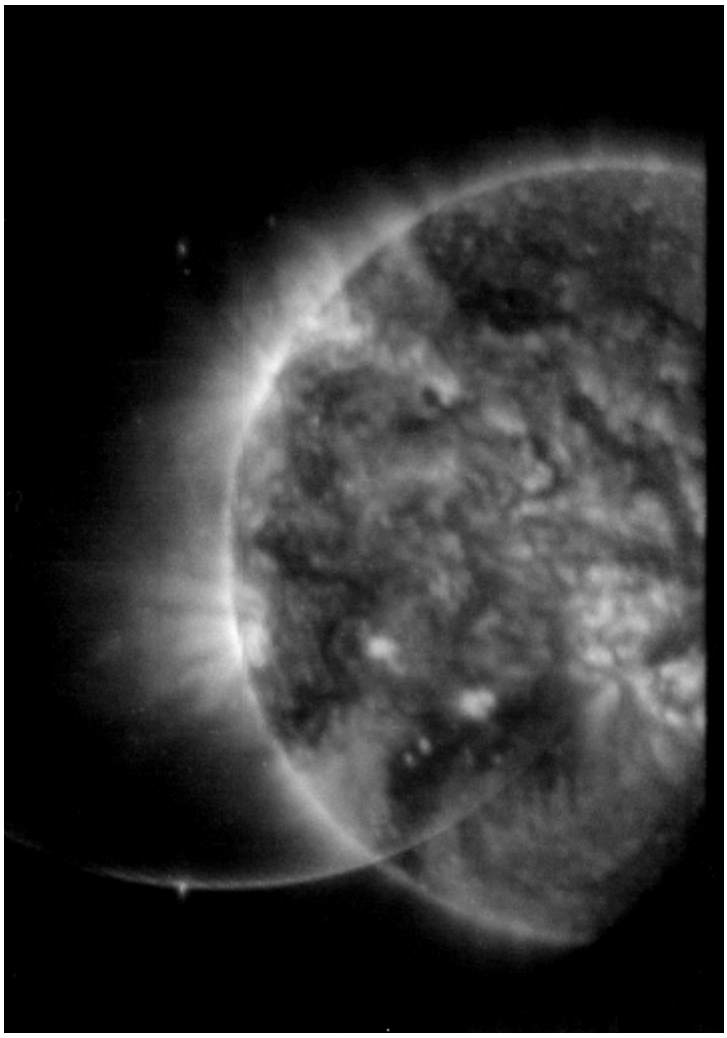

Figure 54. Image from the 150 Å Ritchey-Chrétien telescope.

150 Å Ritchey-Chrétien

This telescope shows the worst misalignment of any of the MSSTA images; the mediocre resolution, analysis of its interferograms, and the fact that the solar disk is significantly off-center and cut by the edge of the film frame all indicate that the primary is tipped in its cell. The limited range of adjustment in the design of the Ritchey-Chrétien optical tubes prevented us from fixing this misalignment. There is also a bright ring of scattered light indicating inadequate baffling of the telescope. Nevertheless, despite these flaws and the confusion about the exact shape of the bandpass, this image is extremely interesting: it is the first image of the solar atmosphere at this wavelength, and the first detailed large-scale view of the solar atmosphere in a line whose peak formation temperature is ~700,000 K.

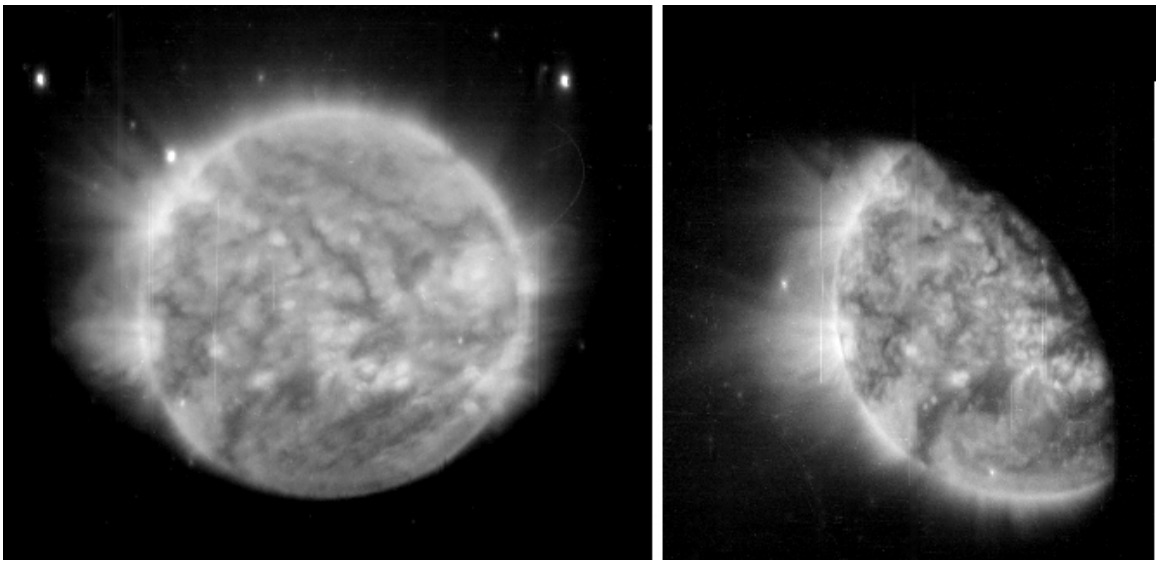

Figure 55. Images from the small Ritchey-Chrétien telescopes at 171 Å (*left)* and 180 Å *(right)*.

171 Å Small Ritchey-Chrétien

This telescope had the worst image resolution of any of the telescopes that recorded images due to the stress on its secondary mirror; however, it produced extremely high contrast, and provided full-disk views in 14 different exposures. It is useful for cross-calibration with TRACE and EIT. There is mild vignetting by the baffle tube at the bottom (south) edge of the disk.

180 Å Small Ritchey-Chrétien

The good (film-limited) resolution performance of this telescope was somewhat offset by the misalignment of its baffle tube, which obscures roughly 40% of the area of the disk. The bandpass is interesting as a bridge between the 171 Å and 195 Å bandpasses; it is another wavelength at which this MSSTA image is the best ever taken.

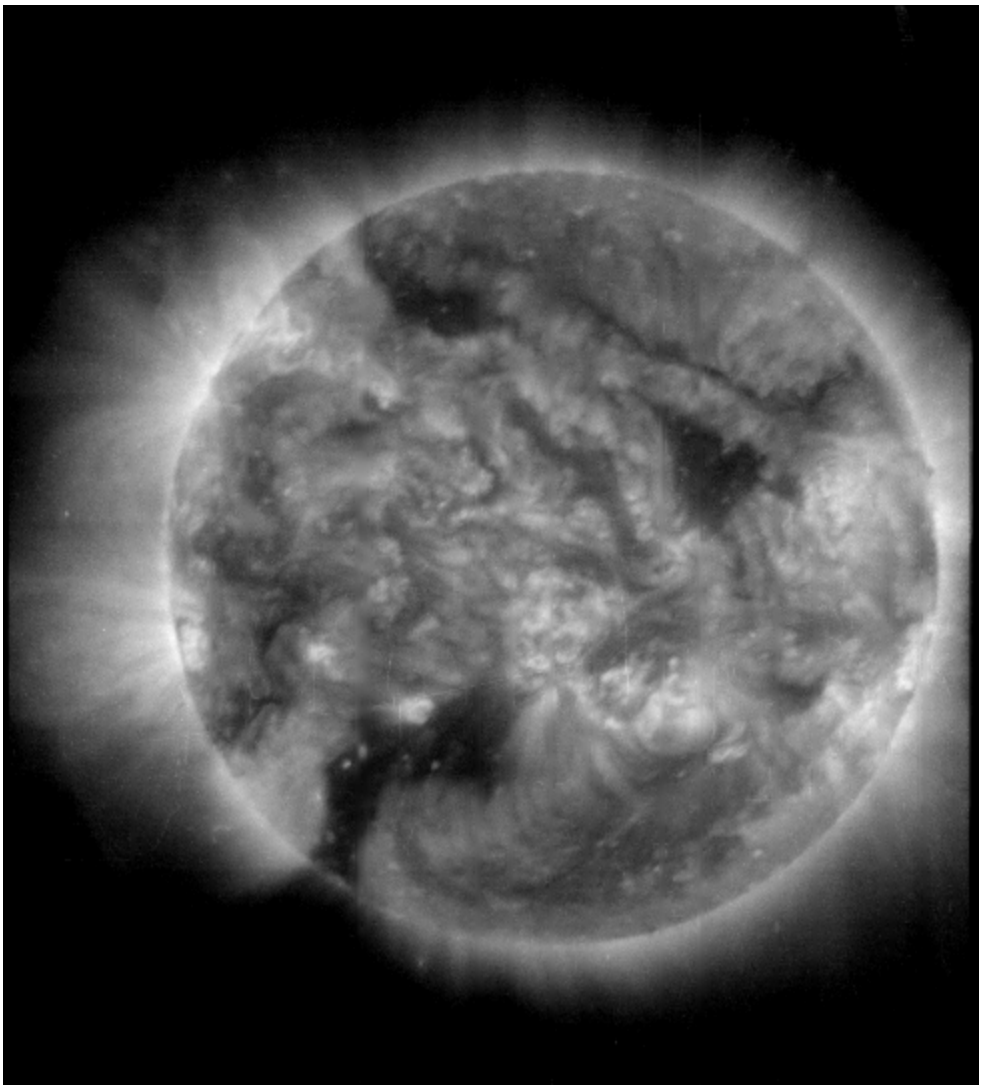

Figure 56. Image from the 195 Å Large Ritchey-Chrétien telescope.

195 Å Ritchey-Chrétien

This telescope provided excellent film-limited resolution and full-disk coverage comparable to the EIT 195 Å telescope. It recorded 14 images, including several short 5-10 second exposures shortly after the opening of the payload's shutter door. This bandpass was used as the reference during image co-alignment and sub-region extraction.

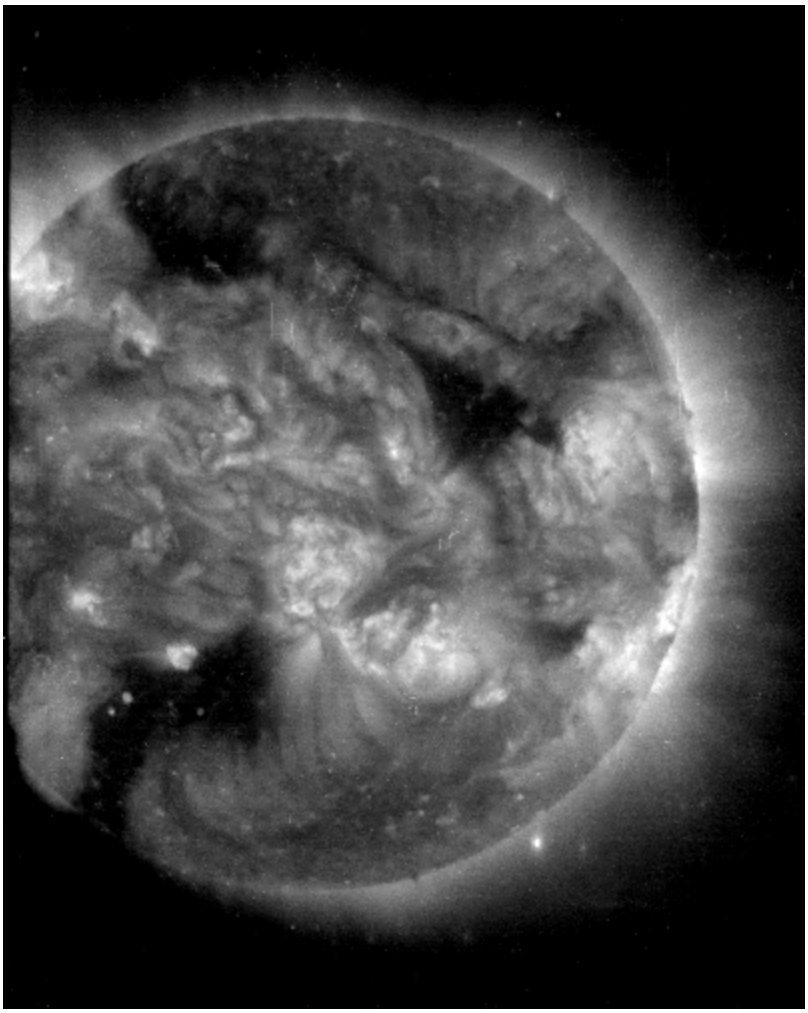

Figure 57. Image from the 211 Å Ritchey-Chrétien telescope.

211 Å Ritchey-Chrétien

The 211 Å telescope had the best resolution of any of the MSSTA EUV telescopes during pre-flight testing, and its images are comparable in sharpness to the 195 Å images. This bandpass, centered on a strong Fe XIV line and serving as a good temperature bridge between the 195 Å and 284 Å bandpasses used by TRACE and EIT, has been flown before (Sakao, Tsuneta et al. 1999), but the MSSTA III image is the highest-resolution 211 Å image ever recorded.

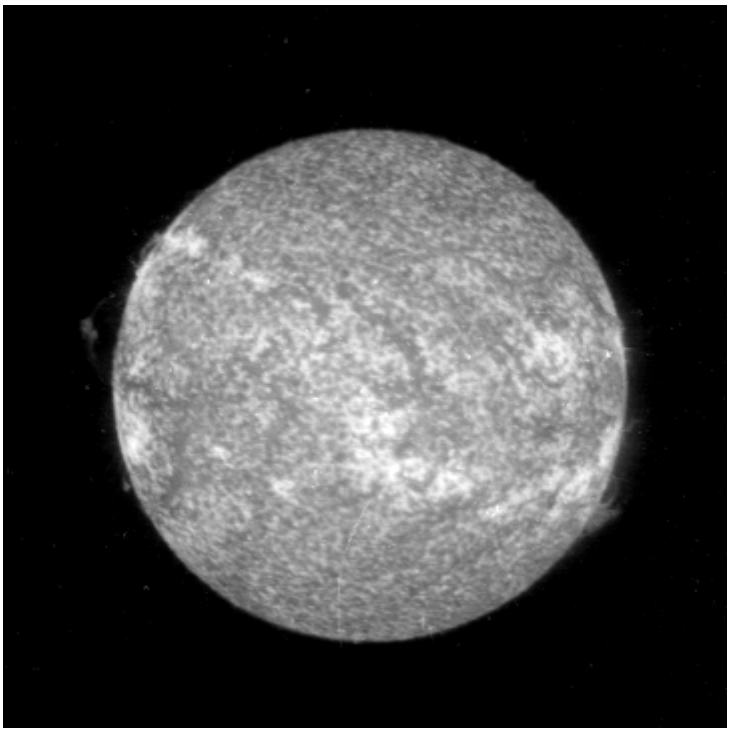

Figure 58. Image from the 1216 Å Ritchey-Chrétien telescope.

1216 Å Ritchey-Chrétien

The short Ritchey-Chrétien Lyman α telescope produced 10 very detailed images, thanks to the extremely fine-grained S-649 emulsion used in its camera. These images show a number of intriguing off-disk loops, and offer the potential for some interesting work. They could be used to explore the connection between coronal and chromospheric structures, and to cross-calibrate the TRACE 1216 Å bandpass.

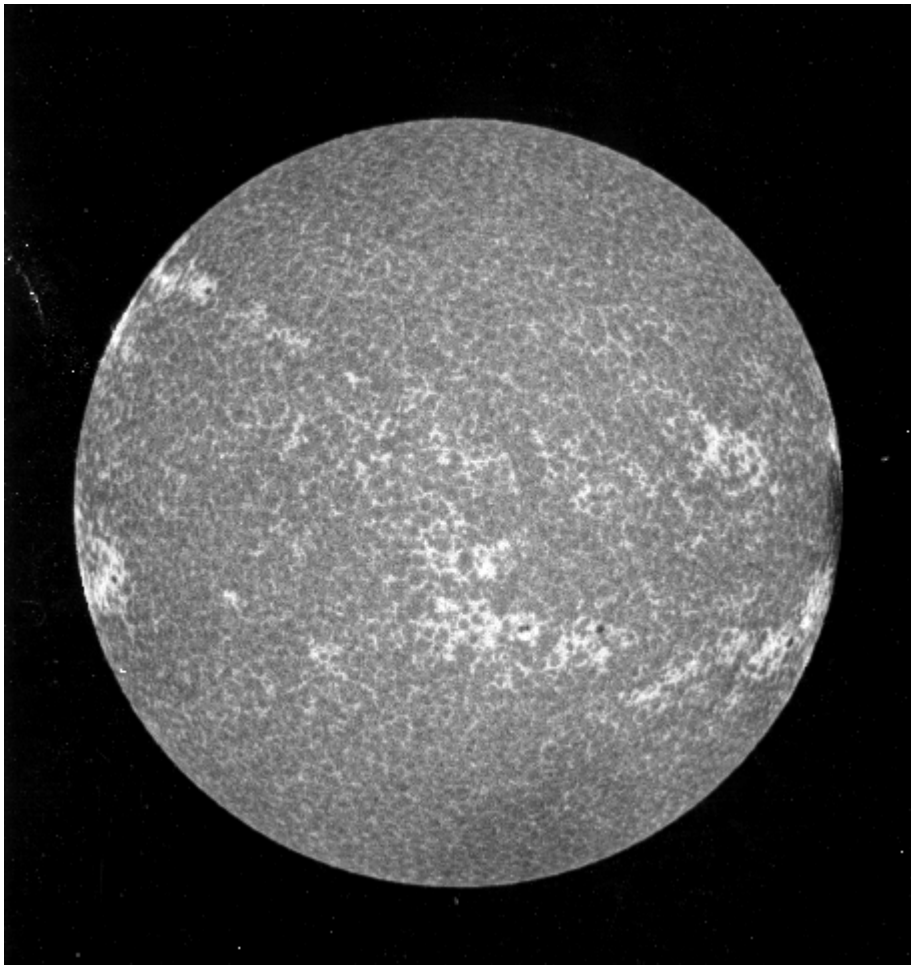

Figure 59. Image from the 1550 Å Ritchey-Chrétien telescope.

1550 Å Ritchey-Chrétien

The resolution in this bandpass is the best of any of the MSSTA telescopes, close to 1 arc-second. The image shows a detailed map of the supergranular network, as well as some bright emission in active regions coming from C IV at 100,000 K. Images in this bandpass or similar ones flown on TRACE are frequently used as proxies for the magnetic network; however, quantitative analysis of such images is difficult because of the strong continuum component in their throughput.

3.3 Post-Flight Calibration

3.3.1 ATMOSPHERIC ABSORPTION

Solar EUV emission is absorbed in the Earth's thermosphere (by atomic and molecular oxygen and ozone, and to a lesser extent by nitrogen), the atmospheric layer that extends from about 90 to 500 km in altitude. At its apogee of 270 km, the MSSTA is well above the point at which most of the absorption takes place. Nevertheless, absorption of ~200 Å radiation begins at altitudes of 400 km, and can be significant at the altitude of the MSSTA. Previous MSSTA flights have not corrected their data for atmospheric absorption. However, because of our concern with precise calibration, and because of the availability of new data and models of the thermosphere, we did attempt to correct the MSSTA III data.

Column densities of the absorbing particles in the atmosphere were computed using the MSIS90 atmospheric model (Hedin 1991), via an IDL interface designed by Don Woodraska of LASP. The model uses the solar 10.7 cm flux as a proxy for overall levels of EUV emission in describing the state of the thermosphere. From the column densities, the absorption coefficient $\mu(\lambda, h)$ of the atmosphere was tabulated as a function of wavelength and altitude over the range explored by the MSSTA.

We determined the altitude of the payload as a function of time *h(t)* based on the known time and altitude at apogee and on the assumption that the payload followed a ballistic trajectory (this assumption is validated by the flight event log in the appendix). Then, for each exposure *j*, the overall atmospheric correction coefficient was found by integrating the atmospheric absorption at the central wavelength of the bandpass from the start time of the exposure to the time the shutter closed:

(Equation 18)
$$\mu_{\lambda,j} = {}^{1}\!\!\diagup\!\!{}_{\Delta t_j} \int_{t_0}^{t_0+\Delta t_j} \mu(\lambda, h(t))\mathrm{d}t$$

Correction factors were of order 5-10% for most of the MSSTA EUV exposures, implying that this is a crucial step if we hope to achieve reliable results. The accuracy of the MSIS90 model is estimated to be ~20-30%; as this factor is primarily associated with the neutral density of the thermosphere, it should show appear as a constant scaling factor in all wavelengths. Thus, the correction introduces a systematic error of a few percent into the absolute accuracy of the MSSTA observations, with a lower error in their relative accuracy.

3.3.2 COMPARISON WITH PREVIOUS EXPERIMENTS

To this day, the only full-disk absolutely-calibrated spectrum of the sun in the 50-300 Å region with sufficient spectral resolution to resolve individual emission lines is the one measured by (Malinovsky and Heroux 1973) in 1969. Therefore, we will use their results as a sanity check on the MSSTA observations. It is worth noting the Malinovsky *et al.* did not correct their spectra for atmospheric absorption; their observations were recorded at around 240 km in altitude, so absorption is likely to be significant at about the 10% level. However, before adjusting the measurements of Malinovsky *et al.*, we note that the 2800 MHz radio flux, often used as a proxy for overall EUV emission (Rugge and Walker 1974), was approximately 11% higher on the day their spectrum was recorded than on the day of the MSSTA flight. These two effects should essentially cancel each other out to within the errors of the observations.

It is possible to check Malinovsky *et al.*'s spectrum against the contemporary measurements from the TIMED-SEE satellite (Woods, Rodgers et al. 1999), which records total irradiance in 10 Å spectral bins. Summing the spectrum of Malinovsky *et al.* to the same bins, adding a small offset for the EUV continuum and lines not included in their line list, and comparing with the TIMED results gives us Table 14. TIMED-SEE measures a solar EUV flux that is notably higher than that reported by Malinovsky *et al.*; the variations among the bins are due to omissions in the line list, or to variations in the detailed shape of the spectra.

Center of 10 Å wavelength bin [Å]	M&H line fluxes plus continuum [10^{-2} ergs cm^{-2} s^{-1}]	Ratio TIMED-SEE/ M&H
145	5.13	1.14
155	5.96	0.76
165	5.42	1.75
175	18.85	2.32
185	19.31	1.30
195	16.54	1.09
205	7.41	2.39
215	9.26	0.93
225	5.73	1.58

Table 14. Comparsion of the full-disk spectrum of (Malinovsky and Heroux 1973) with that measured on the day of flight by TIMED-SEE.

The spectrum of Malinovsky *et al.* was then folded through the bandpass of each of the MSSTA instruments in order to predict the energy that would have been deposited at the instrument's film plane had it observed the full solar disk emitting the measured spectrum. The predictions were compared to the energy summed over all the pixels in each MSSTA image. Because the scanning, alignment and calibration of the MSSTA images is a laborious process, only ~4 different exposures from each bandpass were included in this analysis. The results are summarized in Table 15. The noise estimates based on repeated sampling in the MSSTA images are not too discouraging; most of the observed variation is probably due to scratches in the film or turn-on at extremely low pixel values which are not observed by the shorter exposures, but overall the variance is in line with our expected calibration accuracy. However, it is immediately obvious that the MSSTA observations contain substantially less flux than we would have predicted based on spectral observations; indeed, they are low by factors ranging from 6 to 25!

Central Wavelength [Å]	Number of Measurements	ΔE/E	Ratio MSSTA/M&H
150	4	0.07	0.12
171	3	0.29	0.14
180	4	0.14	0.17
195	5	0.23	0.04
211	4	0.36	0.09

Table 15. Full-disk fluxes observed by the MSSTA telescopes compared with those predicted based on the spectrum of (Malinovsky and Heroux 1973).

3.3.3 COMPARISON WITH THEORETICAL PREDICTIONS

Clearly, this is unacceptable. It is difficult to reconcile these results with the exacting calibration work described in Chapter 2. While it is conceivable that there are large errors in the observations of (Malinovsky and Heroux 1973), it is not possible that they are so far off. They have been qualitatively verified by comparison with TIMED-SEE and numerous other measurements since their publication. The bulk of the discrepancy must come from improper calibration of the MSSTA. The most likely culprit is the film calibration, perhaps during the development time correction phase (see Section 2.5.4). However, re-examination of the calibration film did not eliminate the discrepancy.

We can get a better idea of where the MSSTA observations are diverging from the predictions, and to what extent, by looking at subregions on the disk. For this purpose, the MSSTA images were co-aligned with a set of full-disk EIT images taken roughly 45 minutes earlier. I then identified a sub-region of the EIT images containing an active region whose average flux in the EIT bandpasses agreed with the flux predicted based on the CHIANTI active region DEM (which is itself based on the spectral observations of (Vernazza and Reeves 1978); thus, the chosen sub-region should have a very similar temperature structure to those they observed). The same was done for a quiet-sun region. Then the pixel values in the MSSTA images were averaged over those same sub-regions, using the technique described in Section 4.2.2. The results are shown in Table 16.

Central Wavelength [Å]	Quiet Sun ΔE/E	Quiet Sun Ratio Observations/ Predictions	Active Region ΔE/E	Active Region Ratio Observations/ Predictions
MSSTA				
150	0.19	0.78	0.08	0.55
171	0.30	0.19	0.25	0.16
180	0.18	0.16	0.20	0.17
195	0.24	0.12	0.20	0.10
211	0.18	0.14	0.18	0.10
EIT				
171		1.01		1.01
195		1.02		1.02
284		1.06		1.02

Table 16. MSSTA observations of a quiet-sun region and an active region are compared with predictions based on the CHIANTI DEMs extracted from the spectra of (Vernazza and Reeves 1978). In order to ensure that the selected sub-regions were well-represented by those DEMs, their extent was defined in order to produce good agreement with the predicted EIT observations.

Again, the noise level in the MSSTA images is acceptable, but the overall scale factor is certainly not. It is clear that a correction must be applied to the MSSTA observations in order to bring them into line with the existing body of larger data. This is a bitter blow; one of the major goals of the MSSTA was to offer independently calibration measurements of the solar EUV emission, and to have to renormalize its data to produce agreement with EIT and older spectral observations defeats that purpose. Furthermore, the fact that it is not clear why this correction is necessary is worrisome, and suggests that, even after the MSSTA data have been corrected, their reliability is suspect. What is clear is that the correction is not entirely due to errors in CHIANTI, since the same procedure was used to generate the EIT temperature kernels that offer such good agreement with the predictions. In order to renormalize the MSSTA data in a sensible manner and reassure ourselves of its validity, we must make some assumptions about where this error comes from.

Systematic Renormalization

If indeed the film calibration is to blame, then it is equally to blame in all the MSSTA EUV bandpasses. That is, if we decide to generate a new film calibration transfer function in order to bring the MSSTA observations into line with those from EIT, it must be applied to all MSSTA images. This is the preferred method of renormalization. In order to define the correction to the film calibration, we regridded the EIT images to the same pixel scale as the MSSTA observations. We then examined the ratio of the MSSTA 171 Å images to the EIT 171 Å images, and MSSTA 195 Å to EIT 195 Å, on a pixel by pixel basis.

The procedure is identical to the development time and wavelength corrections described in Section 2.5.4. A fourth order polynomial function, like Equation 15, was fit to optimize the agreement between the MSSTA and EIT pixels in the 171 and 195 Å bandpass. This polynomial was then applied to every MSSTA image in every bandpass during film calibration. It results in an increase in the observed pixel values by an average factor of 8.21.

Arbitrary Renormalization

Alternately, we can simply give up on identifying the source of the error, and simply do the best we can to bring the images in line with our expectations by applying an *ad hoc* scale factor to each image based on the comparisons in Table 16. The easiest way to do this is to simply average the ratios in the active and quiet regions for each bandpass and divide all the images in that bandpass by the average ratio (thus scaling the MSSTA images by a factor ranging from 5, in the case of the 150 Å telescope, to 9 for the 195 Å). This produces the best agreement with the CHIANTI standard DEMs, of course, but it is the most troubling from a theoretical standpoint. In particular, it suggests that we are manipulating our data in order to achieve the outcome we desire.

If we consider the CHIANTI DEMs accurate representations of the conditions in the plasma used for the renormalization, and if we believe that the CHIANTI data used to generate the MSSTA temperature kernels is reliable, then perhaps such a manipulation can be excused. However, particularly in the case of the 150 Å telescope, those assumptions questionable, and if we make them we lose the ability to identify fundamental flaws in the DEM extraction technique. It may be reasonable to enforce agreement between the MSSTA 171 Å and 195 Å bandpasses and the EIT versions of those same telescopes; but then taking the next step and forcing the MSSTA 150 Å telescope to agree with predicted observations without similar experimental verification is more difficult to justify.

Some examinations were made using arbitrarily renormalized data; however, the bulk of the analytical work described in the following chapter is based on data renormalized with the film calibration correction explained above.